Chemical Communications

# Photonic Features of Blue Phase Liquid Crystals Under Curved Confinement

Received 00th January 20xx,
Accepted 00th January 20xx

DOI: 10.1039/x0xx00000x

Jeremy Money[1], Juan G. Munguia-Fernández[2], Sepideh Norouzi[1], Mohsen Esmaeili[1], Jose A. Martinez-Gonzalez[2], Monirosadat Sadati[*1]

Blue phase (BP) liquid crystals represent a fascinating state of soft matter that showcases unique optical and electro-optical properties. Existing between chiral nematic and isotropic phases, BPs are characterized by a three-dimensional cubic lattice structure resulting in selective Bragg reflections of light and consequent vivid structural colors. However, the practical realization of these material systems is hampered by their narrow thermal stability and multi-domain crystalline nature. This feature article provides an overview of the efforts devoted to stabilizing these phases and creating monodomain structures. In particular, it delves into the complex relationship between geometrical confinement, induced curvature, and the structural stability and photonic features of of BPs. Understanding the interaction of curved confinement and structural stability of BPs proves crucially important for the integration of these materials into flexible and miniaturized devices. By shedding light on these critical aspects, this feature review aims to highlight the significance of understanding the coupling effects of physical and mechanical forces on the structural stability of these systems, which can pave the way for the development of efficient and practical devices based on BP liquid crystals.

## 1. Introduction:

In the early 19th century, Friedel made remarkable contributions to the study of liquid crystals (LCs) by introducing them as a mesomorphic state of matter exhibiting both liquid and solid properties simultaneously.[1,2] This "hybrid" behavior arises due to the anisotropy of their molecular units, ultimately giving rise to unique features such as birefringence, dielectric, and diamagnetic properties.[1,3–5] LCs are found among organic compounds with a variety of chemical structures, such as acids, azo- or azoxy-compounds, and cholesteric esters. While behaving as fluids, LCs possess a partial molecular orientation, resulting in the formation of distinct mesophases or mesomorphs, which Friedel introduced to describe the intermediary phase states. These phase states develop according to the anisotropic structure of the LC molecular subunits, or mesogens, and include the nematic, smectic, or chiral phases (Fig. 1A-C).[6–8] When LC molecules are in the nematic phase, they only demonstrate long-range orientational order along their long molecular axis, known as the local nematic director **n**(**r**) (Fig. 1A). On the other hand, smectic LCs show both orientational and positional order, exhibiting layered structures analogous to those seen in conventional solid crystal phases (Fig. 1B).[1,2,9,10]

Chirality, or "handedness", can also be induced within LC mesogens through two primary methods (Fig. 1C). One common approach to inducing chirality in LCs is through the direct incorporation of a chiral center into the mesogens. This is often achieved by asymmetrically replacing one or more carbon atoms within the core molecular structure during synthesis. Another approach involves the introduction of a chiral dopant to achiral mesogens, forcing them to orient at a fixed angle relative to their neighboring molecules (Fig. 1C). The ability of a dopant to induce chirality is characterized by its helical twisting power (HTP). The HTP of a given dopant is inversely related to the concentration of the chiral compound through HTP = $\frac{1}{(c)(p)}$, where $c$ and $p$ represent the concentration of the chiral dopant and a characteristic pitch length, respectively. The pitch length, the parameter to measure the strength of the chirality $q = \frac{2\pi}{p}$, defines the distance over which the local nematic director, **n** completes a full 2π rotation (Fig. 1C).[11–13] Chiral nematic LCs, also referred to as cholesteric LCs, are considered one-dimensional (1D) photonic crystals when their pitch length corresponds to the wavelengths of visible light.[14–

1. Department of Chemical Engineering, College of Engineering and Computing, University of South Carolina, Columbia, SC, 29208, United States
2. Facultad de Ciencias, Universidad Autónoma de San Luis Potosí, Av. Parque Chapultepec 1570, San Luis Potosí 78210, SLP, México.

Electronic Supplementary Information (ESI) available: [details of any supplementary information available should be included here]. See DOI: 10.1039/x0xx00000x

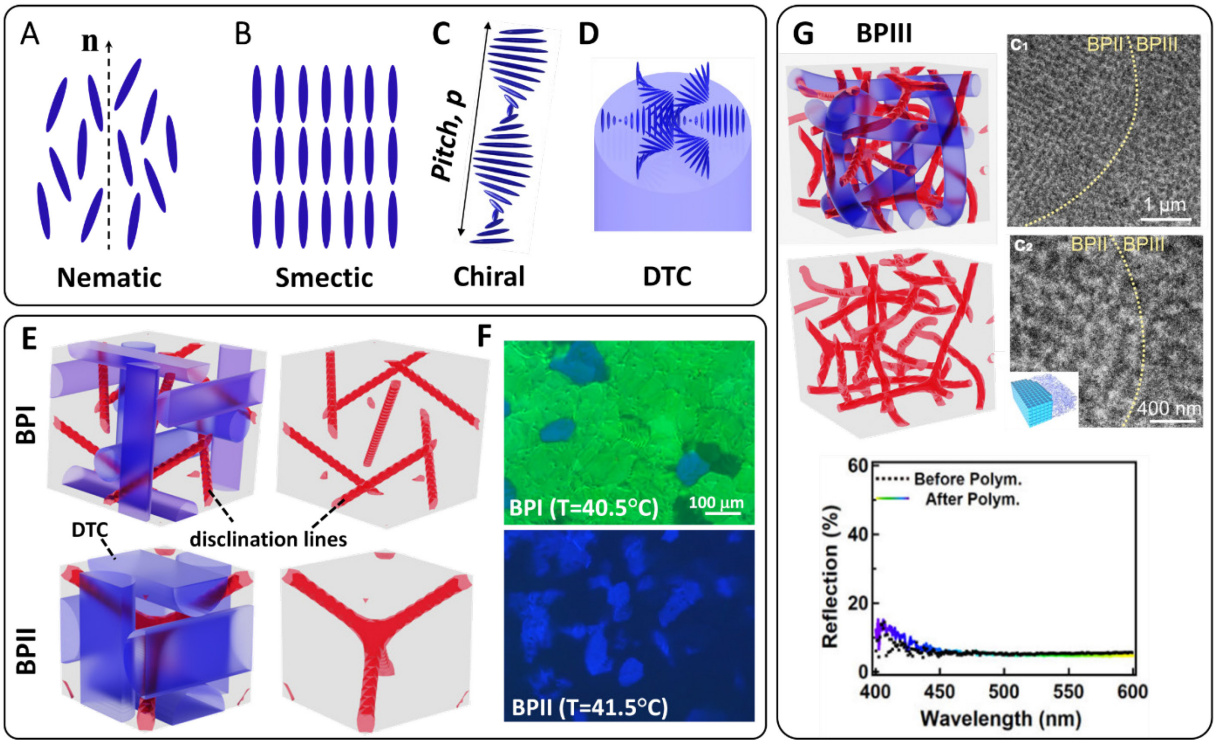


**Fig. 1** A) Nematic LCs with orientational ordering relative to a local director, **n**. B) Smectic LC ordering, with both positional and orientation degrees of order. C) Chiral LC ordering with a characteristic pitch length, *p*. D) Schematic representation of LC ordering in a double twisted cylinder (DTC). E) Cubic packing symmetries of DTCs (Left) for both BPI and BPII along with the formation of their respective disclination lines (Right). F) BP textures of films observed under crossed-polarized optical microscopy. Panel F was reprinted with permission from ref. 39. Copyright 2021 American Chemical Society. G) Simulation of BPIII amorphous network of disclination lines (Top) and TEM images of polymer stabilized BPIII, with reflection spectra showing a lack of birefringence (Bottom). Panel G. was adapted under a Creative Commons CC-BY License from ref. 30. Copyright 2021 Springer Nature.

[9] The reflection wavelength can be represented as $\lambda=np\cos\theta$, indicating a correlation between the pitch length $p$, refractive index $n$, and the angle of light incidence $\Theta$.[20–22]

In thermotropic LC systems, both the orientation and degree of order of the individual mesogens respond to temperature fluctuations. At the vicinity of the cholesteric-isotropic phase transition, systems with high levels of chirality ($p < 500$ nm) show a reduction in total free energy through the self-assembly of so-called double-twisted cylinders (DTC). Within these meso-structures, the directors twist biaxially, exhibiting a helical alignment along two orthogonal directions. Subsequently, these DTCs increase their stability by packing into 3D cubic lattices with unit cells of several hundred nanometers, attaining a thermodynamically stable Blue Phase (BP) (Fig. 1 E). Due to topological constraints, areas between adjacent DTCs contain defects where the molecular orientation and director field **n** cannot be defined. These defects converge to form energetically unfavorable disclination lines, which interpenetrate the cubic structure, thereby limiting the thermal stability window of BPs to 0.5 – 2°C. Upon cooling from the isotropic phase, chiral LCs can assemble into as many as three distinct phases. These phases can be described by the DTC packing symmetries, with BPIII displaying an amorphous network of DTCs, BPII displaying simple-cubic (sc) symmetry, and BPI displaying body-centered-cubic (bcc) symmetry (Fig. 1E).[23–27] While the latter two phases have been extensively studied both computationally and through experiments, BPIII has remained somewhat elusive due its complexity, transient nature and the experimental challenges associated with its characterization. It has been qualitatively described as a "blue fog", since traditional experimental observation techniques such as polarized optical microscopy have remained ineffective due to the lack of birefringence or brag scattering of the amorphous network. However, computational studies combined with electron micrograph experiments provide confirmation on the topological landscape of this phase (Fig. 1G).[28–32]

As both BPI and BPII exhibit cubic symmetries with lattice parameters corresponding to the wavelength range

 

of visible light, their inherent topologies achieve an adjustable photonic bandgap. This bandgap results in selective reflection of specific wavelengths, giving BP materials their characteristic iridescence and vivid colors. This phenomenon can be described by Bragg's equation, $\lambda = \frac{2na}{\sqrt{h^2+l^2+k^2}}$, where $n$, $a$, and $hkl$ are the material refractive index, BP lattice size and Miller indices of the crystal planes, respectively. As the above equation suggests, the BP lattice size and their orientation are determinant features that control the reflection of visible light.[33] Tunability of these features is desired for downstream technologies and future fundamental studies. As such, examination of the governing equation for HTP calculations suggests the chiral pitch length roughly approximates BP lattice sizes with the following relationship: $p \approx a_{\mathrm{BPI}} \approx 2a_{\mathrm{BPII}}$.[11] This indicates that for a specified chiral dopant, the size of the resultant BP lattice can be controlled through adjustment of the dopant concentration. The chiral pitch length thus serves as a parameter to fine-tune the reflected colors within the spectrum of visible light, allowing for a wavelength shift from blue to red.[34,35]

Among our work, we have shown that BPs share notable similarities with the well-known atomic solid crystals. We find these systems display long-range orientational ordering and evidence of martensitic-like, diffusion-less crystal-crystal transformations with incredibly fast response times.[36-38] One of the unique and attractive features of LCs is their ease of processibility in comparison to their solid counterparts. Typical solid photonic crystals require expensive materials and processing methods to fabricate, such as nanolithography. Instead of these complex and costly processes, BP photonic crystals can be achieved by simply mixing nematic LC components with a high concentration of chiral dopants under relatively mild processing conditions.[11,39] In addition to ease of processibility, the liquid-like nature of LCs allows them to flow and respond to confining geometries, a feature which is not shared with their solid-state crystalline counterparts. This makes them highly suitable for integration into soft or flexible photonic materials, where solid alternatives are not viable. Moreover, the structures, which can be tuned by external stimuli including temperature, electric field, mechanical forces, and chemical and biochemical analytes hold promise for a wide range of applications spanning optoelectronics, photonics, actuators, and chemo/biosensors.[40-49]

While existing as a potentially transformative technology, the commercial realization of BPs still has many hurdles to overcome. To begin with, BPs exist in a very narrow temperature range, preventing widespread use in most practical applications.[11] While the thermal stability window remains qualitatively small, the exact temperature ranges in which BPs form vary greatly depending upon several material-dependent factors, such as chiral dopant concentrations, dopant structure, LC chemistry, and other additives. For example, Emeršič et al. explored three separate material systems exhibiting various BP transition ranges between 30.8-31.1 ºC, 55.6-56.4 ºC, and 75.5-77.0 ˚C.[110] Furthermore, Castles et al. highlighted two systems that exhibited BP transition ranges from 48-50 ˚C and 52.5-54 ºC.[97] In addition to narrow thermal stability windows, BPs are inclined to generate polycrystalline structures in flat films. This suggests the formation of varying orientations of the crystal lattices, and thus grain boundaries, resulting in a reflection of incident light at different wavelengths. Single crystal orientation BPs formed by various surface treatments have demonstrated narrower reflection-band widths, stronger reflectance, and improved electro-optical performance with a significantly lower voltage requirement.[50–54]

The experimental and theoretical research on BPs, including studies related to thermal stability and monodomain formation, are mainly concerned with the bulk properties of the material where the thickness of the BP film is at least 20 times of the BP lattice constant. However, the growing interest in the integration of these ordered materials into miniaturized, flexible devices brings about the need to understand the interplay between spatial confinement, curvature, and interfacial interactions. While there is a dearth of experimental research exploring the effects of strong 2D spatial confinement on BP structures, their inherent stability and topological defects have been extensively explored through theoretical models and computational simulations.[28,55–61] Here, the interaction between DTCs and the energy cost associated with their accompanying disclination lines plays a significant role in achieving a delicate equilibrium in the structure of confined LCs. In addition, the fluid-like nature of BPs provides an ideal system to study the effect of topological constraints induced by curvature on periodic crystalline structures and understand how these constraints influence the organization and structural stability of defects. In this feature article we first delve into the effect of confinement and curvature on the structural stability of BPs. Subsequently, we review the primary challenges associated with realizing BP technologies and highlight

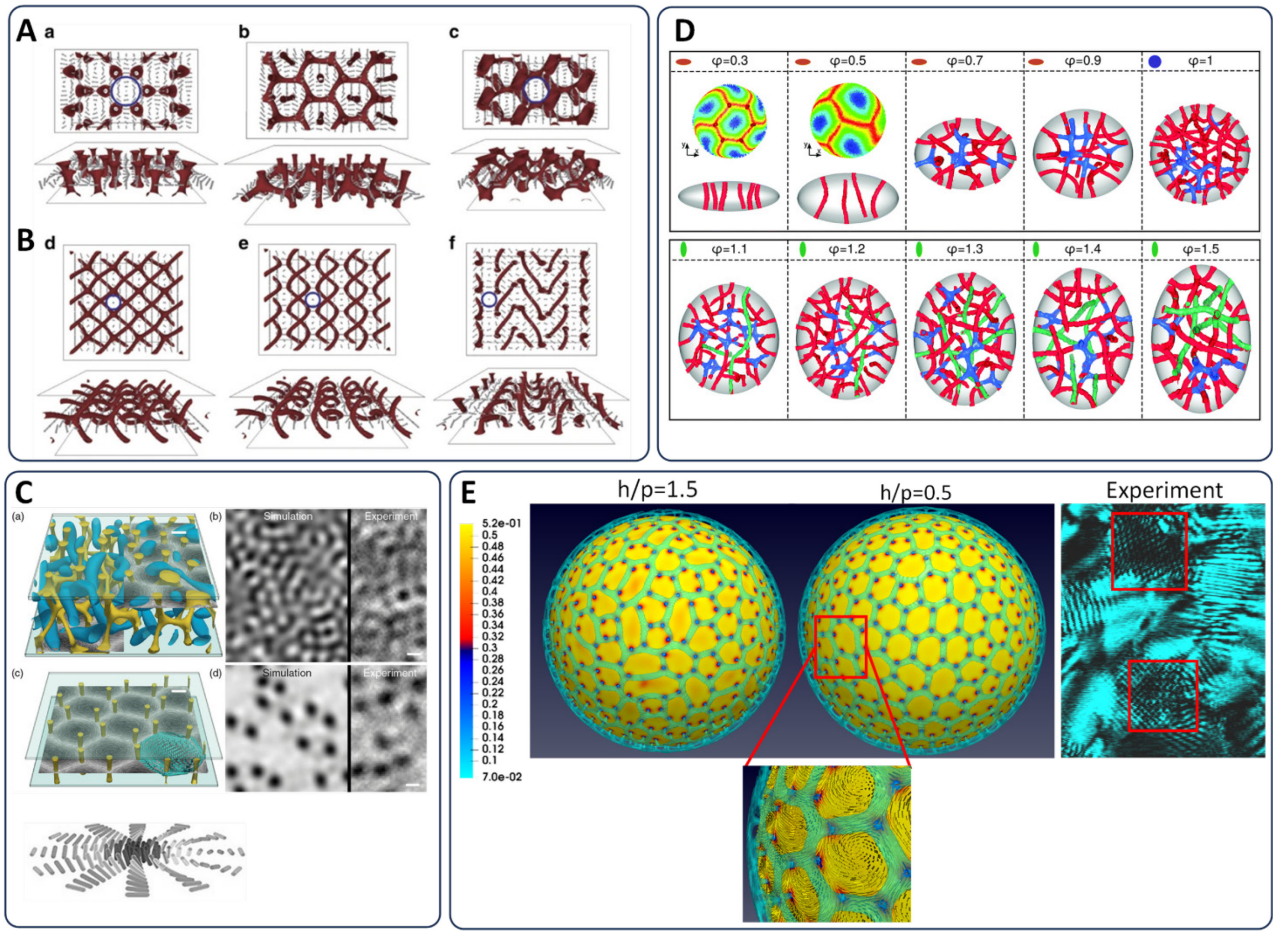


**Fig. 2** A) Simulated Skyrmion disclination network with hexagonal symmetry as a result of parallel plate confinement, and B) an array of double-helix defect lines, two orthogonal sets of parallel winding disclinations, and a regular array of ring defects formed under strong 2D confinement. Panels A and B were reprinted with permission from ref. 56. Copyright 2011 Springer Nature. C) Thin film disclination array of half-Skyrmions between two slides with weak planar degenerate anchoring. Panel C was adapted under a Creative Commons CC-BY License from ref. 28. Copyright 2022 American Physical Society. D) Progression of BPs from spherical to oblate ($\varphi < 1$) to prolate ($\varphi > 1$), with disclination lines either hybridized or converging to form lattice networks. Panel D reprinted with permission from ref. 95. Copyright 2020 Royal Society of Chemistry. E) Simulated isosurface of BPII shells with varying thickness and the super-resolution confocal laser scanning microscopy image taken of a shell with a thickness of 600 nm. Reprinted with permission from ref. 95. Copyright 2022 American Chemical Society.

mitigating strategies with a particular emphasis on the impact of curvature on phase behavior and photonic features of pure and stabilized soft BP crystals.

## 2. Effect of Confinement

### 2.1 BP Structures within 1D Confinement

Understanding the structural stability and optical response of LCs in confined geometries are important subjects both in fundamental science and practical applications such as display technology and flexible electronics. The effect of 1D confinement on the configuration and optical properties of BPs have been extensively studied for BP films with a range of thicknesses, spanning from greater to lesser than the lattice size.[50,56,58,62-65] In the case of BPI and BPII confined in films with a gradient in thickness, both display periodic colors that continuously blue-shift towards regions with lesser thickness.[62,66] This effect was attributed to the strain-induced by the confining geometry. In fact, when bulk BPs are confined between parallel plates with a thickness smaller than the lattice parameter, the characteristic length scale, *p*, and 3D packing of the DTCs compete with the linear dimensions of the confining space. Under such conditions, LCs can manifest a plethora of configurations and distinct disclination line topologies, indicative of their adaptive response to spatial restrictions.

Through computational simulations, Fukuda and Žumer have explored the interplay of geometrical confinement and surface anchoring conditions on the intriguing disclination networks that arise in BPs.[56,57,58,

 

[60,64] They have shown that in thin films, BP disclination networks reconfigure to stable, quasi-two-dimensional (2D) Skyrmion lattices with hexagonal or rectangular symmetry. The term "Skyrmion" refers to vortexlike organizations of gradually ordered chiral LC molecules absent of any singularities at the center. Skyrmion structures with hexagonal symmetry are particularly intriguing (Fig. 2A, B). For BP films thinner than the lattice constant of bulk BPs, a 2D hexagonal lattice of half-Skyrmion excitations forms within an array of -1/2 topological defects (Fig. 2A).[56,57,60] The formation of Skyrmion lattices in BPs relies upon high levels of chirality, accurate temperature control—preferably near the isotropic phase transition—and a notably thin film with strong surface anchoring conditions.[56] By further varying the system temperature, simulations confirm the existence of exotic ordered structures including an array of double-helix defect lines, two orthogonal sets of parallel winding disclinations, and a regular array of ring defects[56–58,67] (Fig. 2B). These observations highlight the need for further experimental studies aimed at both validating and confirming the resultant textures of Skyrmion lattices within confined LCs.

Recently, Muševič and co-workers demonstrated the formation of a hexagonal lattice of half-Skyrmions in thin LC films between two surfaces with weak planar degenerate anchoring (Fig. 2C).[8,59,60] The LC materials were prepared by mixing nematic LC ZhK-1289 and a chiral dopant CB15, which has been shown to form BPI with a lattice size of 360 nm. They employed high-resolution microscopy coupled with Kossel analysis to both confirm and characterize the half-Skyrmion textures. While the resultant architecture was previously predicted with theoretical simulations, the initial conditions of these simulated systems assumed the confining surfaces to have homeotropic anchoring. In turn, this subsequent work led to the conclusion that anchoring conditions at the system boundaries influence the mechanism by which these half-Skyrmion architectures propagate and stabilize. Confining surfaces with homeotropic anchoring were found to stabilize the director field at the centers of the half-Skyrmions, while planar-degenerate anchoring assists with the stabilization of the disclination lines that are perpendicular to the surfaces.[8,59,60]

## 2.2 BP Structures in Curved Confinement

A long-standing topic in LC research surrounds the interplay between bulk properties and surface effects in confined geometries. The liquid-like nature of LCs allows them to easily accommodate different confining geometries, creating distinct and fascinating networks of topological defects. As such, alteration of the geometric

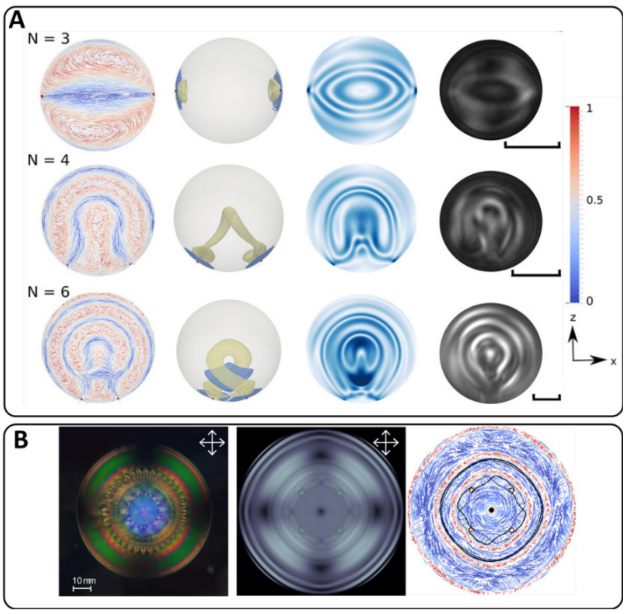


**Fig. 3** A) Left to right: resulting simulation snapshot of isosurfaces of director field (blue) and point defects (red) within droplets after altering the ratio of the droplet radius to LC pitch length. Splay (blue) and bend (yellow) distortions in droplets. Polarization graphs for light incident along the y-axis. Corresponding experimental images taken from droplets of differing chirality. Panel A was reprinted with permission from ref. 87. Copyright 2016 American Chemical Society. B) (left) Crossed polarized micrograph of a 60 µm oblate LC droplet with a high level of chirality. (center and right) Polarization micrograph and director field obtained from Landau-de Gennes simulations. Panel B was adapted under a Creative Commons CC-BY NC License from ref. 34. Copyright 2020 The American Association for the Advancement of Science.

features of the confining boundaries of these systems serves as an effective tool to control the orientation of LC molecules and their resultant topological defect network. While the respective director field orientation results from a sensitive interplay between interfacial and bulk properties,[10,68-71] the formation of unique defect networks are a direct result of the topological restrictions imposed by confining boundaries and any associated curvature.[10,70–74] Numerous experimental, theoretical, and simulation studies have focused on the origin of this structural diversity and established a detailed picture of the director field configurations in nematic, smectic, or chiral LCs when confined in different geometries such as droplets, cylinders, shells, and tori. Confinement of nematic LCs in spherical geometry, for example, can lead to two distinct director field configurations. A radial morphology with a point-like defect at the center of the droplet appears when the interface forces homeotropic anchoring, whereas a bipolar configuration with two point-defects at the poles (boojums) can form if the interface induces planar anchoring. Nematic and smectic

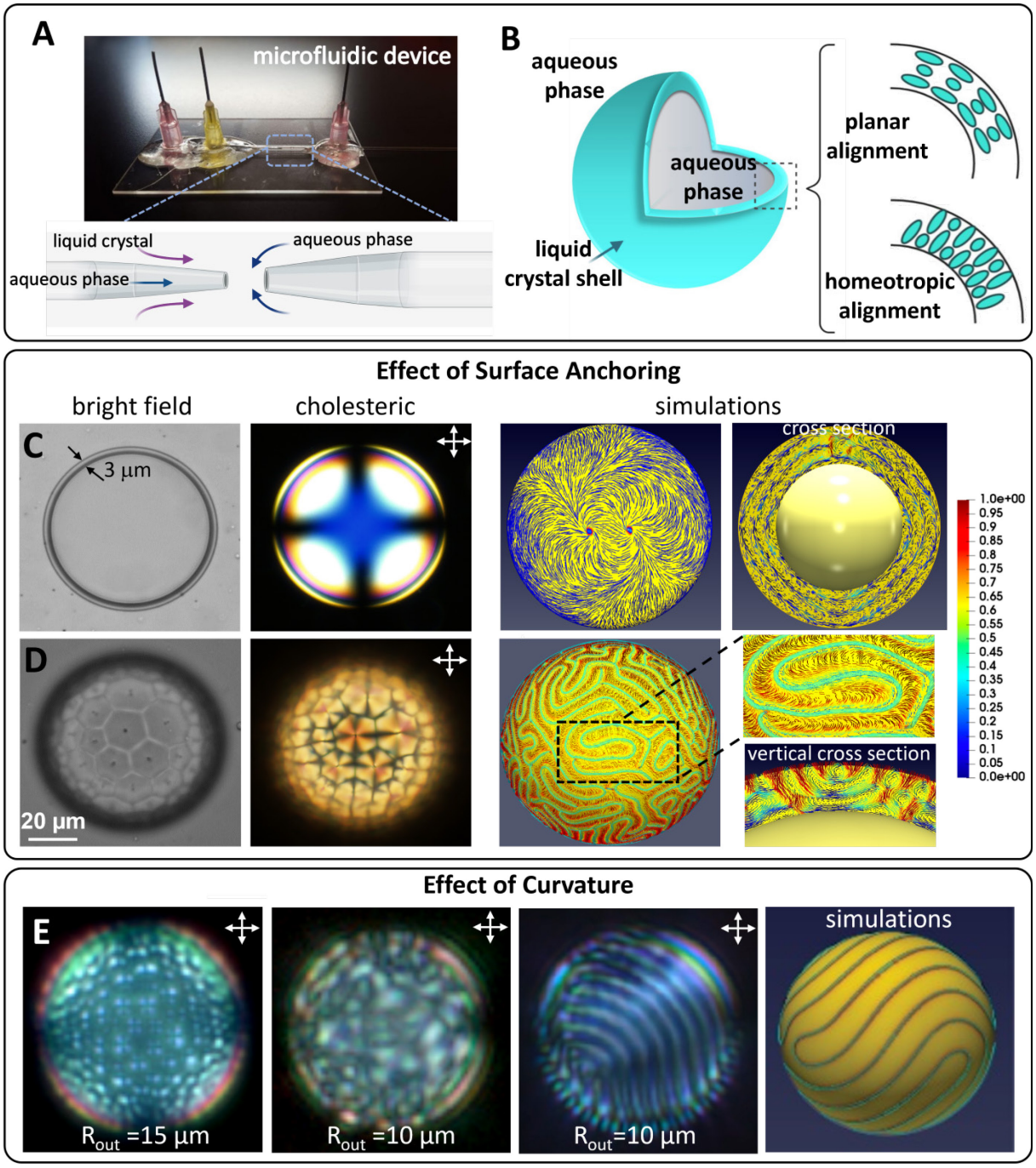


**Fig. 4** A) Microfluidic device setup for fabrication of core-shell LC droplets. B) Schematic representation of LC anchoring conditions at inner and outer core surface boundaries. C-D) Effect of surface anchoring: Bright-field micrographs of cholesteric shells (left). Reflection-mode cross-polarized micrograph of 3 µm thick shell (center) and top and cross-section views of computationally simulated director fields (right) on the planar surface and in focal conic domains. E) Effect of curvature: From left to right: 15 µm outer radius droplet. 10 µm droplet showing change in texture with increasing temperature in the cholesteric phase. Simulation of disclination networks within core-shell droplets. Panels A through E were reprinted with permission from ref. 92. Copyright 2022 American Chemical Society.

LCs confined in cylindrical capillaries have also been explored both experimentally and computationally. Under homeotropic anchoring conditions, these systems exhibit an escaped radial (ER) structure, where the director escapes from radial ordering toward the major cylindrical axis when approaching the center. With planar anchoring conditions, the structure exhibits broken rotational symmetry with two +1/2 line defects along the major cylinder axis, commonly referred to as Planar Polar with two Line Defects (PPLD). [75–79] Both the shape and size of the confining surfaces can strongly influence the alignment of LC molecules. For example,

 

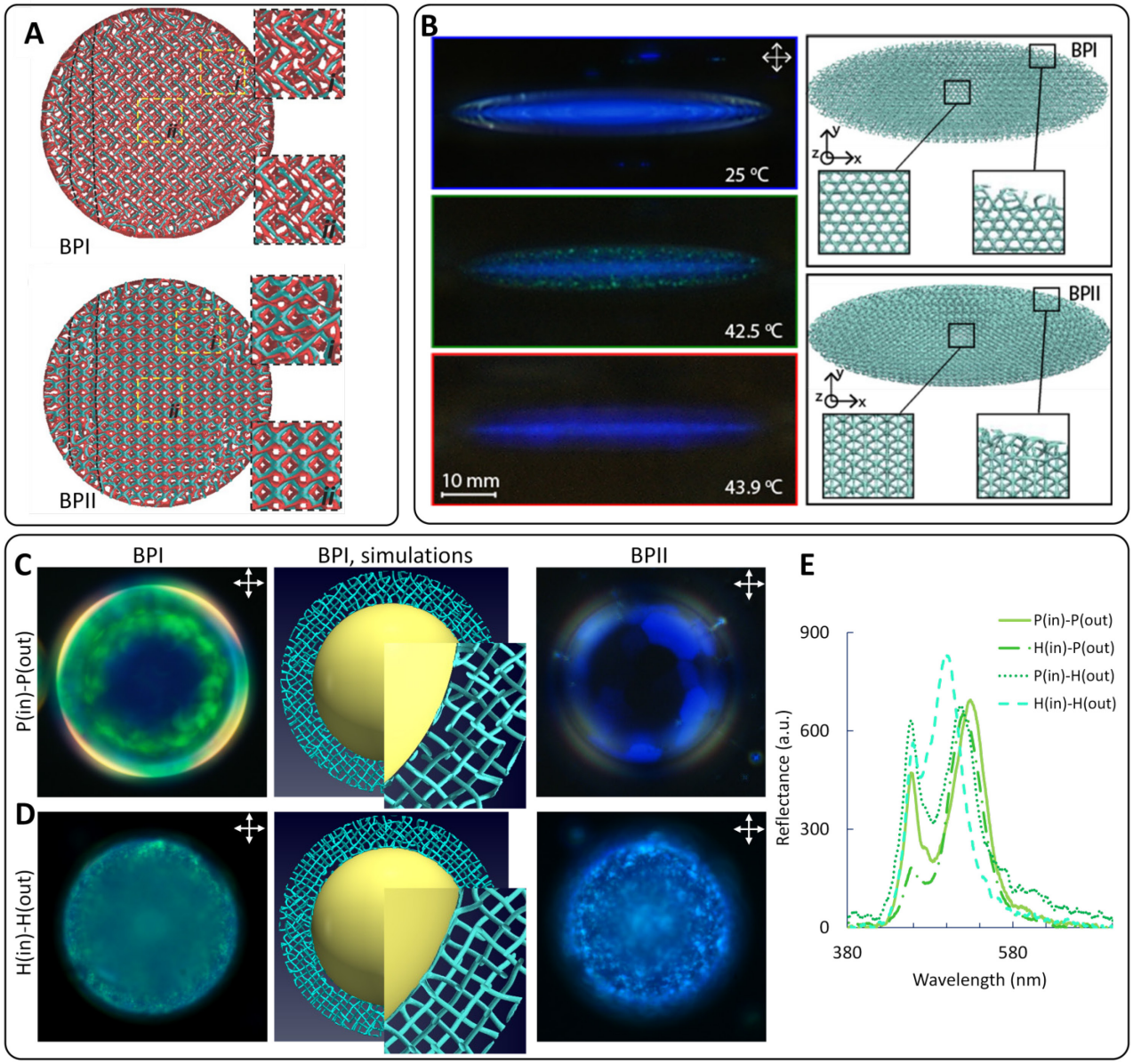


**Fig. 5** A) Simulated BPI (Top) and BPII (Bottom) disclination networks in droplets. Panel A was reprinted with permission from ref. 94. Copyright 2015 John Wiley and Sons. B) Reflection mode crossed-polarized optical microscopy images of stretched LC droplets with high level of chirality under varying temperature conditions (Left) and their corresponding simulated networks of disclination lines (Right). Panel B was adapted under a Creative Commons CC-BY NC License from ref. 34. Copyright 2020 The American Association for the Advancement of Science. C-D) Reflection mode crossed-polarized optical microscopy images of BPI (right), BPII (Left) shells and the simulation snapshots of networks of disclination lines in BPI shell (middle) under varying homogenous anchoring conditions. E) Reflectance spectra of confined BPI in core-shell droplets with differing anchoring conditions. The spherical shells in experiment have the outer diameter and thickness of approximately 90 µm and 3 µm, respectively. Panels C through E were reprinted with permission from ref. 92. Copyright 2022 American Chemical Society.

when confined in spherical droplets, Abbott and co-workers have observed changes in the ordering textures of 5CB director fields with decreasing droplet sizes. As the droplet diameters decreased from 3µm to 1µm and then to 700 nm, the resultant director fields established bipolar, pre-radial, and radial ordering, respectively.[80]

Chiral LCs are particularly sensitive to distortions associated with curvature and the proximity of interfaces.[11] As a result, the coupling of curvature, size and surface anchoring conditions can foster the formation of increasingly complex chiral assemblies.[81–83] Chiral LCs confined in spherical droplets exhibit defect structures that arise from the interplay of the inherent twist configuration of the mesogenic arrangements and the curvature imposed at the droplet surface. This relationship is defined by the $p/R$ ratio, where $p$ and $R$ are

the pitch of the cholesteric and the radius of the sphere droplet, respectively (Fig. 3A).[84-88] Yoshioka et al. have stabilized a single helix and double twisted structure in microdroplets by tuning the LC helical pitch length and droplet diameter.[89] Through a combination of theory and experiment, Zhou et al. reported that increasing the level of chirality of LCs confined in micrometer-sized droplets with planar anchoring could lead to a continuous transition from a twisted bipolar structure to a radial spherical structure (RSS, Fig. 3A).[87] In addition to this, Posnjak et al. reported the creation of a new structure, reminiscent of 2D Skyrmions, in microdroplets by imposing homeotropic anchoring conditions.[90] Seč et al. simulated spherical cholesteric droplets with degenerate planar anchoring, and varying levels of chirality relative to the droplet diameter ($N=\frac{4R}{p}$, where N is the number of $\pi$ turns the director makes in a non-confined cholesteric along the distance of the droplet diameter, 2R).[82] The numerical calculations revealed three known structures: radial spherical (RSS), diametrical spherical (DSS) and planar bipolar structures, exhibiting defect regions which deviated from nematic systems. These structures offered varying ranges of stability relative to the droplet radius-to-pitch ratio, with RSS favoring larger radius to pitch ratios (N>4), DSS favoring smaller radius to pitch ratios (N≤4), and planar bipolar structures remaining metastable state across all N (Fig. 3A).[82] By relying on both experiments and computational simulations, we have also demonstrated that the coupling of curvature, elasticity, and strain on the chiral LC confined in oblate cavities can lead to the emergence of new molecular configurations and a palette of morphologies including RSS and diametrical oblate structures (DOS). These structures each contain distinct topological line defects, forming a series of single unlinked loops and knot-like molecular configurations (Fig. 3B).[34]

Spherical shells have also been utilized as a suitable platform to investigate the coupling of bulk elasticity, confinement, and surface anchoring in chiral LCs. Microfluidic technology has enabled precise control over the shell diameter (curvature) as well as the anchoring condition on both the inner (core) and outer (shell) surfaces (Fig. 4A, B). In addition, the shell thickness can be finely adjusted through the osmotic swelling process to independently examine the confinement effect. The structural arrangements of chiral LCs with a low level of chirality and thereby large cholesteric pitch length in core-shells have been extensively studied. For example, Darmon et al. observed an RSS composed of two intertwined defect lines in planar-aligned chiral shells.[91] They achieved this by tunning the confinement ratio ($h/p$), where $h$ denotes the thickness of a spherical shell and $p$ represents the cholesteric pitch. Furthermore, utilizing the adaptable platform offered by shell geometry, Tran et al. reported the emergence of stripe patterns and focal conic domains on the shell surface of a LC with low level of chirality when the surface alignment transitions from planar to homeotropic orientation.[83] We have expanded this research and recently explored how the interplay between confinement, curvature, and surface anchoring in a core-shell geometry influences the structural arrangement and optical properties of LCs with high levels of chirality (Fig. 4).[92] When these systems enter the cholesteric phase (at room temperature), enforcing planar anchoring on both the outer and inner surfaces of the shells positions the twist axis of the mesostructures perpendicular to the droplet surface. This orientation leads to a radial structure which, when viewed under a polarized microscope, manifests as a cross pattern (Fig. 4C). On the other hand, homeotropic surface anchoring causes molecules to orient perpendicularly to the interface leading to the twist axis aligning parallel to the surface (Fig. 4B). This configuration conflicts with the in-plane molecular orientation of the bulk, forming focal conic domains on the outer surface (Fig. 4D). Axisymmetric focal conic domains were also observed on the outer surface of shells that employ hybrid surface anchoring—featuring differing molecular organizations at the inner and outer surfaces (Fig. 4D). In these patterns, the director field displays an RSS near the inner degenerate planar interface. This configuration, however, shifts dramatically near the outer homeotropic interface, resulting in the formation of +1/2 disclination lines. Increasing the degree of curvature and confinement transitions the focal conic patterns into bent stripe patterns (Fig. 4E).[96,97] These diverse and dynamic spatial patterns, evident in cholesteric shells, offer considerable potential for the further development of engineered colloidal assemblies.

At higher temperatures, when a system with a high level of chirality self-assembles to form BPs, previous numerical and computational research have identified structural reconfiguration in cubic lattice structures under curved confinement. For instance, recent work has shown the deformation of disclination lines upon approaching the curved surface, ultimately affecting the reflected wavelength of visible light (Fig. 5A).[33, 94] They further demonstrated that within curved geometries featuring weak planar anchoring, BPs exhibit a greater degree of stability compared to their behavior in bulk conditions. In prolate microdroplets, on the other hand, we identified the emergence of two distinct regions as the transition temperatures of BPs are approached (Fig. 5B).[34] In these regions, the outer areas exhibit BP characteristics at a

 

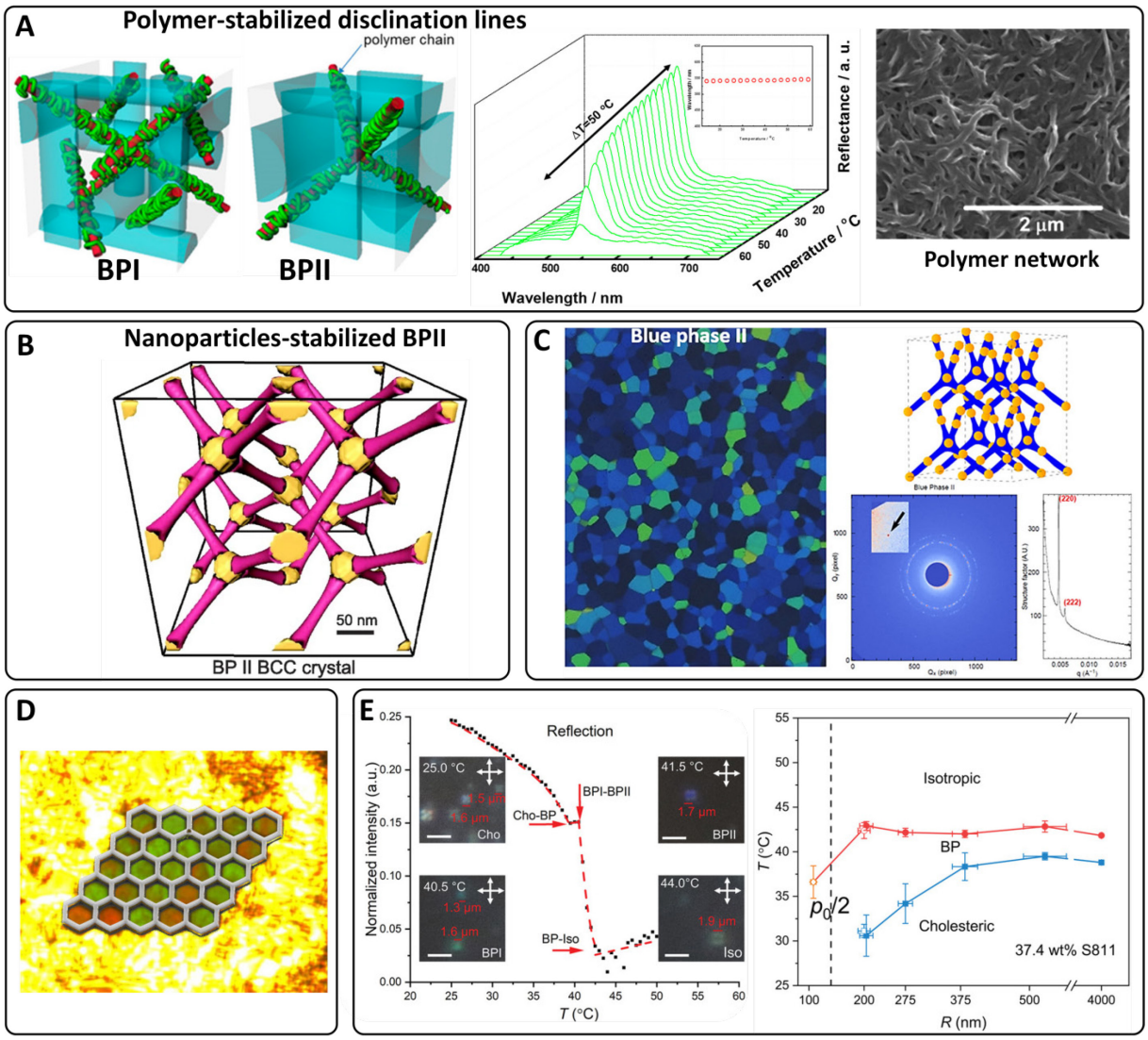


**Fig. 6** A) Schematic representation of cubic packing symmetries and the resultant disclination lines, with polymer chains reducing the core volume of these high energy regions (Left). The resultant stable phase range of polymer stabilized BPs (Center). SEM image of resultant polymer network of a free-standing polymer stabilized disclination network (Right). Panel A was reprinted with permission from ref. 102. Copyright 2017 American Chemical Society. B) Simulation of nanoparticle infused LC system and the resultant location of the migrated nanoparticles into the central region of disclination lattices. Panel B was reprinted with permission from ref. 103. Copyright 2011 National Academy of Sciences. C) Poly-domain platelet textures of nanoparticles stabilized BPII templates. Panel C was reprinted with permission from ref. 104. Copyright 2016 American Chemical Society. D) Microwells produced by direct ink writing inducing confinement. Panel D was adapted under a Creative Commons CC-BY License from ref. 106. Copyright 2018 American Chemical Society. E) Phase diagram of BP systems and their resultant reflection spectra at a given system temperature (Left). Phase regions as a function of confinement radius, showing a widening of stable temperature ranges for BPs with smaller radii (Right). Panel E was reprinted with permission from ref. 35. Copyright 2022 John Wiley and Sons.

lower temperature relative to the inner core. This was attributed to the possible structural evolution and modifications in the BP-lattice periodicity induced by the interfacial strain (Fig. 5B).[34]

In submicrometric scale droplets, major changes to the BP cuboidal lattice structures, such as new arrays of defect lines and hexagonal patterns begin to arise.[37] These results demonstrate that while alteration of anchoring strength influences defect core topology, destabilization of the entire morphology of the material was more directly related to droplet size. In a similar line of study, numerical simulations demonstrated that the cuboidal structures of BPs within oblate cavities transform into half-Skyrmions, and the geometrical constraints imposed by the prolate spheroid leads to hybridization of these BPs (Fig. 2D).[95]

When confined in shells, BPs show intriguing behaviors. In our recent work, we have systematically examined these conditions using experimental measurements and computational simulations.[92] We have shown that the geometric incompatibility between curved boundaries and the 3D cubic structure of BPs constrains the arrangements of disclination lines, leading to the formation of new and exotic structures. We have explored the effect of coupling shell thickness, curvature, and surface anchoring on the optical properties, phase behavior, and configurational order of BPs. We identified a noticeable blue-shift in the reflectance spectra of BPI confined in shells with homeotropic anchoring, which is directly proportional to area of the interface (Fig. 5C-E). We employed computational simulations based on a mean-field Landau–de Gennes formalism to gain a better understanding of how the interplay between the curvature-induced strain and homeotropic surface anchoring affects the arrangement of disclination lines in BP shells. Our results show that when confined in shells with homeotropic anchoring, disclination lines in BPI bend and form junctions when approaching the surface of the droplet (Fig. 5C-D). In the case of BPII, however, the reflected color was independent of the surface anchoring and remained unchanged, which is attributed to the integrity of its disclination network. Instead, the size of the BPII crystal platelets diminished, and the multi-domain characteristic of the BPII became more prominent (Fig. 5C-D).

We further explored the effect of confinement and curvature on the structural stability and optical response of BPs by systematically decreasing the shell thickness and outer diameter. Our experimental observations coupled with computational simulations showed that increased confinement and curvature leads to a decrease in the stability of BPI, causing it to restructure into BPII.[92] The structural instability of BPI can be explained by its larger lattice size and disjointed defect lines. Upon further reducing the shell thickness (approximately to twice the pitch length), the disclination lines in BPs transformed into Skyrmion lattices. These changes were detected using super-resolution confocal laser microscopy imaging when the shell thickness was reduced to approximately 600 nm (Fig. 2E). Our computational simulations also accurately predicted this structural transformation, confirming that the interplay between curvature and confinement facilitates the formation of Skyrmion lattices in shells with greater thicknesses compared to the requirements for flat films (Fig. 2E).[92]

## 3. Stabilization of BPs

As previously mentioned, BPs typically manifest within a very narrow temperature range. Many efforts have been undertaken to increase the stability of these phases, such as the inclusion of nanoparticles, polymer networks, or modulating the confining geometries. For instance, optical switching for display applications requires stability in room temperature, and in order to address this issue the use of polymeric networks have been shown to significantly enhance the thermal stability window of many LC material systems.[102] Reactive bi-mesogenic systems have been shown to stabilize BPs through the formation of templated polymer networks, reaching temperature ranges as broad as 250 ºC. [97] Similar approaches to address hysteresis effects associated with polymer stabilized systems involve generating, washing, and refilling polymeric networks with nematic LCs.[111] Nevertheless, expanding the thermal stability of BPs in general has been achieved through two different approaches, 1) stabilizing disclinations lines, and 2) confining BP crystals. Here we review these two approaches and the techniques used to primarily stabilize BP structures along with combined approaches to further optimize these material systems. Specifically, we will delve into the relationship between confinement and curvature and the impact of this coupling on the structural stability of BPs based on our latest research findings.

### 3.1. Stabilization of Disclination Networks

Considering that disclination lines are areas of maximal free energy, Kikuchi and his team proposed that incorporating additional components into these lines could effectively reduce the free energy cost associated with defects, thereby enhancing the stability of BPs over an expanded temperature range.[96] They studied the effect of varying monomer composition and concentrations on the stability windows of BPI LCs. It was hypothesized that random coils of polymer chains can localize in the core of disclination lines and perturb the arrangements of the adjacent LC molecules, lowering the thermal energy requirements of the core to maintain its isotropic liquid state (Fig. 6A). This in turn led to a stabilized lattice network of disclination lines, which guides and further stabilizes the orientation of the surrounding LC molecules under lower thermal conditions (Fig. 6A).[96] The group also showed that a fine balance of miscibility between the host LC and monomer additives must be achieved to create a stabilization effect, as highly compatible LC monomers showed no increase in thermal stability due to the homogenous distribution throughout BP host liquid crystalline material. Many researchers

 

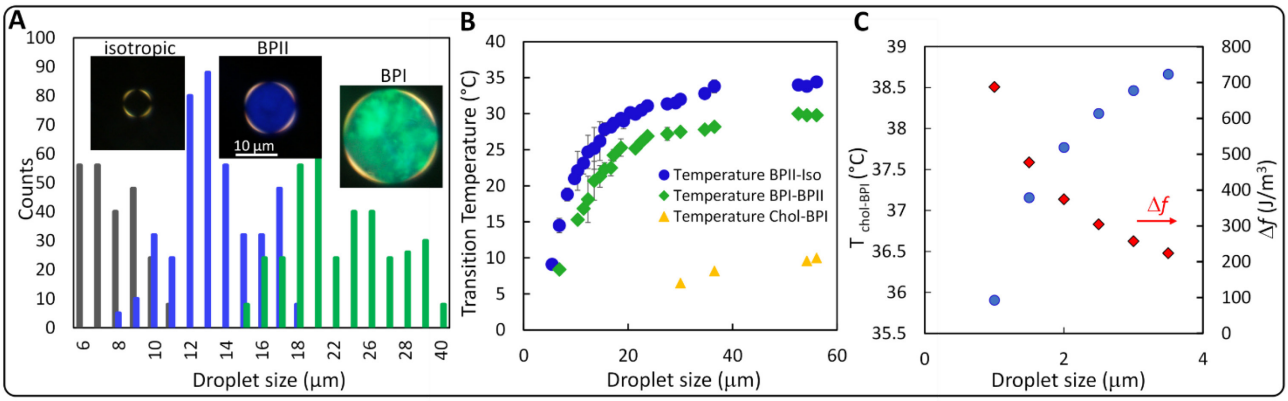


**Fig. 7** A) Phase distribution of various droplet sizes showing droplet size defines the BP structure stabilized in droplets. B) Phase transition temperatures of BPs as a function of droplet sizes. C) Simulated cholesteric-BP transition temperature as a function of droplet size, and the predicted free energy of the system. Panels A through C were reprinted with permission from ref. 39. Copyright 2022 American Chemical Society.

have utilized the polymer stabilization approach and explored the impact of various factors, such as polymer chain solubility, composition, rigidity, and the degree of cross-link density in BP bulk.[97-101] Following this strategy, Castles et al. created free standing, 3D casting templates with lightly crosslinked polymer networks.[97] Using a 3-5 wt% chiral dopant, 25-50 wt% reactive mesogens/photo initiator mixture dissolved in bi-mesogenic LC, they were able to fabricate a free-standing template which was then washed of liquid crystalline material. Subsequently, they validated the structural integrity of the polymer matrix by refilling the template with an achiral 5CB nematic LC. The templated achiral material was able to successfully achieve a BP like structure with a characteristic reflection pattern reminiscent of BPI oriented in the [011] crystalline direction. When filled with a large temperature range achiral nematic (BL006 Merck), they achieved an unchanging optical response from -125 °C to 125 °C, dwarfing conventional BP systems.[97] In the same line of study, Jo et al. introduced low concentrations of monomers Trimethylolpropane Triacrylate (TMPTA) and reactive mesogens 2-Methyl-1,4-phentlene bis(4-(3-(acryloyloxy)propoxy)benzoate) (RM257) to a chiral nematic LC precursor.[102] After surface treatment of the glass substrate comprising the film's cell (5 µm thickness), the group was able to fabricate LC films with a 60 °C window of stability for BPII. Xiang et al. utilized a polymer-stabilized BP template to fill a broad-temperature nematic (E7).[111] This was to reduce the increased optical switching time normally seen in polymer-stabilized materials. In doing so, they were able to achieve a broad temperature range (130 °C) and optimal switching time (61 to 87 µs) compared to either the pure BP or polymer-stabilized BP alone. Similarly, Lee et al. created multiple formulations of polymer stabilized BP samples, using varying concentrations of PETA (Pentaerythritol tetraacrylate) and SL04151 as the chiral LC material.[112] Holding LC concentrations constant, they found increasing PETA concentrations beyond 3 wt% removed the phase transition to BPII, creating a direct transition route between the isotropic-BPI phases. The effect is potentially due to immiscibility between the non-mesogenic monomer and the liquid crystalline material, favoring migration to the disclination lines and formation of interfaces between the disclinations and liquid crystalline host material. This, in combination with the introduction of the chiral mesogenic monomers SL04151, stabilizes the formation and packing of DTCs thereby improving thermal stability.

Another approach to extend the temperature range of BPs involves the integration of nanoparticles (NPs) into disclination lines. Xu et al. introduced ferroelectric nanoparticles which leveraged the sensitivity of BPs to an applied electric field, simultaneously increasing the clearing temperature window of the system while also reducing the driving voltage by more than 70%.[109] Similar to polymeric inclusions, NPs accumulate within the lattice disclination lines of the BPs, stabilizing the chiral BP structures (Fig. 6B). Gharbi, et al. utilized surface functionalized gold NPs which were miscible in cyanobiphenyl based LCs and observed the resulting cubic structures utilizing polarized optical microscopy and synchrotron small-angle X-ray scattering (SAXS).[104] The addition of the NPs showed distinct textures under polarized microscopy, while the SAXS analysis showed observable peaks indicating cubic ordering of the predicted phase (Fig. 6C). Additionally, the diffuse NPs increased the stability temperature range of the BPs from 0.9 to 2.5 ºC.[104] By dispersing gold spherical nanoparticles on the order of 3.7 nm in a BP mixture, Yoshida et al. were able to increase the temperature

window of BPI from 1°C to 11°C.[105] Similarly, systematic high-resolution studies by Karatairi et al. found that including CdSe NPs treated with hydrophobic oleyl amine and tri-octyl phosphine in S-(+)4-(2'-methylbutyl)phenyl 4'-n-octylbiphenyl-4carboxylate (CE8 or 8SI*) and S-(+)-4-(2-methylbutyl)phenyl 4-decycloxybenzoate (CE6) LCs increased the range in which BPII appeared by up to 20 K for CE8.[113] Mechanistically, the hydrophobic surface functionalization of the NPs drives their localization into the disclination lines. This in turn reduces the free energy penalties associated with the presence of disclination lines, thus furthering the transition temperature between isotropic and BPs.

### 3.2. BP Stabilization Induced by Geometrical Confinement and Curvature

Geometrical confinement of pure BPs has also been shown to impact their structural and thermal stability. Lin et al. have recently shown that confining pure cholesteric LC in a direct ink printed honeycomb microwell reduces the BP transition temperatures to room temperature and expands their thermal stability ranges dramatically upwards of four-fold (Fig. 6D).[101] This is attributed to the weak boundary force provided by the honeycomb walls. In fact, when the chiral LC is cooled down from the isotropic phase, this boundary force coupled with anchoring conditions of the substrate anchors the growth of the soft crystal alignment and provides a barrier to the dissolution of the DTCs, stabilizing BPs over a wider temperature range.

To understand the interaction of geometrical curvature and 3D cubic lattice structure of BPs, we have explored the structural stability of pure BPs in microdroplets through a combined approach of simulations and experimental observation. We studied the effect of surface anchoring strength and the degree of confinement and curvature on the optical responses of BPs and their inherent stability windows.[33] The results showed that tunability of the unit cell size of BPs in droplets was achievable through alteration of the droplet diameter and anchoring strength. Furthermore, these results show that the stability of BPs under confinement was significantly different from that compared to the bulk, as droplets exhibited an increase in the range of stability for both BPI and BPII. In a similar line of study, it was further noted that there was a slight decrease in the transition temperature from isotropic to BPII in droplets with diameters below 4 micrometers.[94] However, little size effect was detected for transition temperatures between BPII-BPI and BPI-cholesteric phases. Yang et al. continued this study, and both experimentally and computationally investigated the structural stability of BPs in sub-micrometer droplets dispersed in an aqueous solution.[35] They developed an optical technique based on light scattering to precisely track the structural evolution in sub-micrometer droplets. Their findings indicated a substantial decrease in the transition temperatures from isotropic to BP as the droplet size reduced to the sub-micrometer range (Fig. 6E). However, the stability window of BP expanded threefold. The free energy analysis of the confined systems showed that the chiral contribution to the elastic energy primarily determines the stability of different phases.[37] Understanding the structural stability and phase behavior of BPs at the sub-micron scale is particularly important as they offer a larger specific surface area, which could be advantageous for applications like sensing and drug delivery.

We have recently explored the coupling effect of curvature and polymer stabilization of disclination networks on the structure and phase behavior of BPs confined in microdroplets.[39] Our studies have demonstrated a strong correlation between the size of the stabilized BP microdroplets and the phase transition temperature (Fig. 7A). These results show that the size of the confining geometry significantly influences the structure and stability of the phase (Fig. 7A, B). After polymerization, droplets having a diameter smaller than 10 μm appeared isotropic, while those with diameters between 11 to 16 μm and larger than 17 μm showed BPII and BPI structures, respectively (Fig. 7A). The BPs were identified through their distinct reflectance peaks using a spectrometry technique, and their associated lattice size was accurately determined using super-resolution laser confocal microscopy. When comparing our observation (Fig. 7B) with the results reported by Yang et al.[35] (Fig. 6E), it is evident that the coupling of polymer stabilization of BPs and the curvature-induced strain can influence the size dependency of phase behavior, leading to its manifestation in larger droplets and at lower temperatures. Nevertheless, the results showed that that the process of polymer stabilization in microdroplets significantly enhanced the stability window of both BPI and BPII by approximately twenty-fold and three-fold, respectively (Fig. 7C).

### 3.3. Theoretical Approach on the Effect of a Guest Component and Curved Confinement on the Stability of BPs

The stability of BPs through the introduction of polymers into the disclination networks can be explained based on Fukuda's work.[107] As mentioned previously, the disclination lines of a BP represent localized regions with the highest free energy density. As a result, introducing a

 

volume fraction, $\phi$, of monomers causes them to aggregate within the disclination lines. Within BPI unit cells, such a monomer aggregation is assumed to form cylindrical regions of volume $\Omega_M$, with anchoring energy, $\sigma$, and area per unit volume, s. As a result, the free energy of BPI that accounts for the monomer aggregation can be written as $F_{BPI}^{mon} = \int_{\Omega_{Tot}-\Omega_M} d\boldsymbol{r}\, f(\boldsymbol{r}) + \Omega_{Tot}(\phi f_M + \sigma s)$. Where $f$(r) is the profile of the free energy density of BPI, $\Omega_{Tot}$ is the total volume and $f_M$ is the free energy density contribution of the monomer. The last term of this equation accounts for the effect of the interfacial energy that depends on the monomer aggregation at the disclination lines. For the cholesteric phase, there are no preferential sites for monomer aggregation due to an absence of disclination lines, therefore, the corresponding free energy is given by

$F_{Chol}^{mon} = \Omega_{Tot}[(1-\phi)f_{Chol} + \phi f_M]$, where $f_{Chol}$ is the free energy density of the pure cholesteric phase. Subtracting these two free energy equations results in $F_{BPI}^{mon} - F_{Chol}^{mon} = \int_{\Omega_{Tot}-\Omega_M} d\boldsymbol{r}\, f(\boldsymbol{r}) + \Omega_{Tot}[-(1-\phi)f_{Chol} + \sigma s]$.

Intuitively, it can be deduced from the net free energy equation that stability of the BPI increases with monomer concentration. Within a BPI-unit cell the straight, disjointed disclination lines that can be seen as 4 diagonals, each of length $\sqrt{3}a_{BPI}$. Therefore, the monomer aggregation produces cylindrical regions of volume $4\sqrt{3}a_{BPI}\pi r^2$ which is equivalent to $\phi a_{BPI}^3$. The area of the interface per unit volume is given by $s = \frac{8\sqrt{3}a_{BPI}\pi r}{a_{BPI}^3} = \frac{4}{a_{BPI}}\left(\sqrt{3}\,\pi\phi\right)^{1/2}$. Hence, by considering the monomer-rich disclination lines as locally isotropic, the free energy gap between the monomer-laden BPI and cholesteric phases depends on the monomer volume fraction as shown by $F_{BPI}^{mon} - F_{Chol}^{mon} = F_{BPI} - F_{Chol} + \Omega_{Tot}\left[(f_{Chol} - f_{iso})\phi + \frac{4\sigma}{a_{BPI}}\left(\sqrt{3}\,\pi\phi\right)^{\frac{1}{2}}\right]$[107,39], where $F_{BPI}$ and $F_{Chol}$ are the free energy of the pure BPI and cholesteric phases. Since the isotropic free energy density is larger than the free energy density associated with the cholesteric phase, the addition of a small amount of monomer stabilizes BPI over the cholesteric phase. Confinement distorts the BP unit cells, particularly near the interfaces, and the effect of confinement on the stability of the BPI can be considered by introducing an average BP-unit cell, $\overline{a}_{BPI}$.

## 4. Controlling the BP-Lattice Orientations

An additional challenge associated with bringing BP technology to commercial realization is the formation of polycrystalline domains. For many directed applications such as opto-electronics and photonic displays, the granular textures associated with multiple crystalline domain orientations increase voltage requirements and decrease optical response times. To overcome this challenge and obtain crystal domains with uniform orientation, chemical and physical treatment of the confining surfaces have been explored as a practical strategy. For example, Zheng et al. developed a method based on a photoalignment technique to produce micropatterns with localized and uniform-oriented BP domains. These patterns can be erased and rewritten by sequential UV-irradiation and electric-field stimulation.[108] By using glass cells which impose weak planar anchoring energy, Oton et al. could obtain large BP-crystals with different lattice orientations.[51] They prepared Indium Tin Oxide (ITO) coated ultra-flat glass substrates that were rubbed in an antiparallel configuration and assembled into sandwich cells 5 to 15 μm thick. Their findings indicate that the lattice orientation of large BP-crystals depended not only on the cell thickness, but also the helical twisting power and concentration product of the chiral dopant.

We used computational techniques to sample the behavior of the preferred molecular alignment on the substrate and identify those regions where the given anchoring conditions impose (or release) strain of the confined BP to produce on-demand lattice orientation (Fig. 8A-C). These continuum simulations have been very useful for guiding the design of the chemical hybrid (homeotropic-planar) anchoring patterns to promote the nucleation and growth of monodomain BPs with controlled lattice orientations. Based on the simulation conditions, the chemical patterns were experimentally produced using e-beam lithography on a Si substrate covered by a uniform poly(6-(4-methoxy-azobenzene-4'-oxy) hexyl methacrylate) (PMMAZO)/OTS layer (Fig. 8A).[50] This surface patterning approach was also exploited to generate sculpted grain boundaries with complex geometries (Fig. 8B).[36]

BP-single crystals grown on chemically pattered surfaces have shown a diffusion-less, martensitic-like transformation during the BPI-BPII phase transition. In solid atomic crystals, the martensitic transformation consists of a cooperative and coordinated movement of atoms that triggers changes in the lattice symmetry of the crystals. In contrast, BP-lattices are orders of magnitude larger than the atomic lattices, and the material is in a liquid state with diffusion events occurring continuously. However, the building units of a BP-lattice are DTCs and these entities do not diffuse but instead exhibit a cooperative and coordinated motion. The martensitic nature of BP crystal transformations was first reported in a work by Li et al., using an epitaxial assembly strategy.

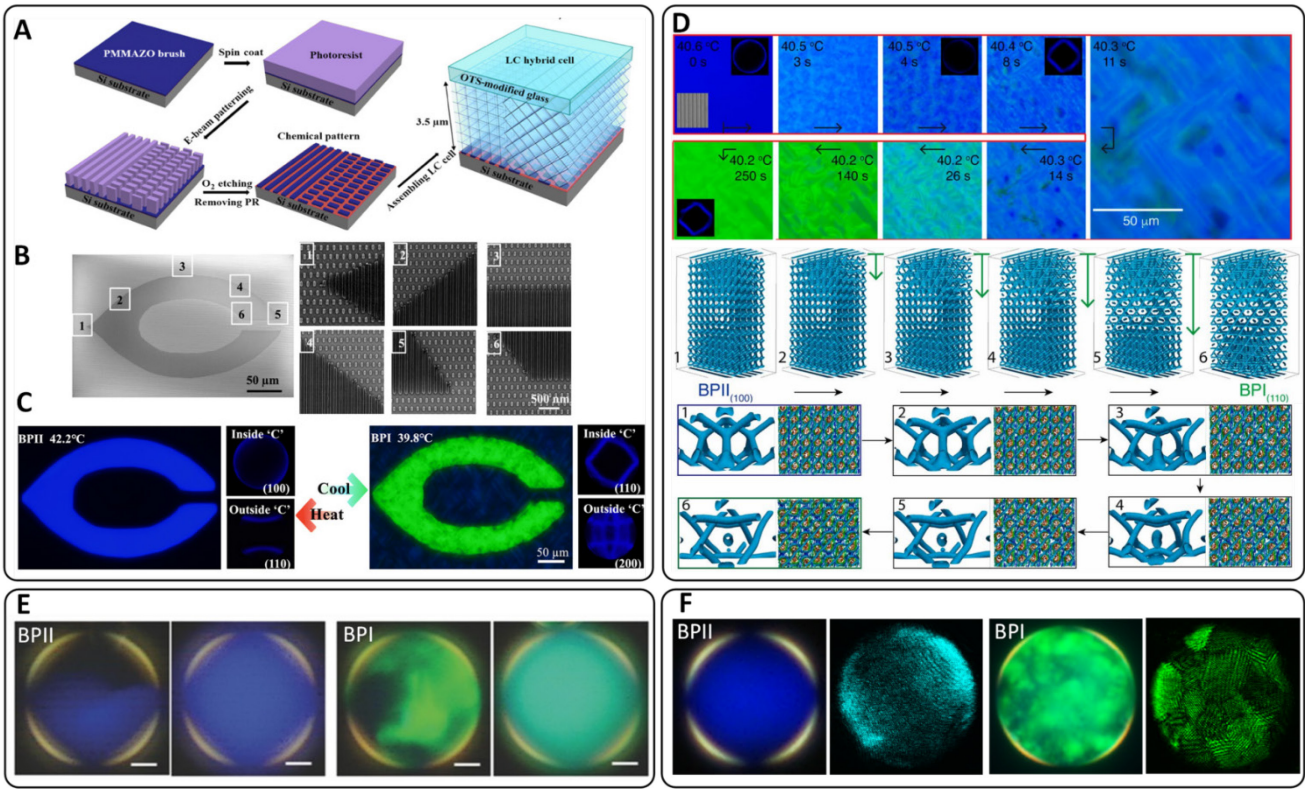


**Fig. 8** A) Schematic representation of the process of fabrication of chemical patterns. B) A dual-patterned surface under SEM imaging. C) Reflection mode polarized optical microscopy images of C patterned surfaces and resultant Kossel Diagrams. Panels A through C were adapted under a Creative Commons CC-BY NC License from ref. 36. Copyright 2019 The American Association for the Advancement of Science. (D) Phase transformation of BPI-BPII transitions upon heating and cooling in a hybrid cell with a striped chemical pattern and snapshots of reconfiguration of topological defect network during BPII-BPI phase transition. Panels D was reprinted with permission from ref. 37. Copyright 2017 National Academy of Sciences. E) Optical characterization of BPII (Left) and BPI (Right) droplets (scale bar is 5 μm). Panel E was reprinted with permission from ref. 94. Copyright 2015 John Wiley and Sons. F) Polarized optical microscopy image of polymer stabilized BPII (Left) and BPI (Right) droplet with corresponding confocal laser scanning microscopy images. Panel F reprinted with permission from ref. 39. Copyright 2021 American Chemical Society.

They found that in a matter of seconds, the system undergoes a transformation between two macroscopic BP single crystals.[37,38] They associated the distinct crosshatched structure that precedes the BPI-BPII transformation as a signature of the underlying crystal reconfiguration process, from SC to BCC, which is characteristic of a martensitic transformation (Fig. 8D). Starting from a BPII with a temperature near the BPII-BPI transition temperature, the Landau-de Gennes formalism was implemented to simulate an annealing process consisting of a slight change in temperature followed by a free-energy relaxation. Consistent with the experiments, the simulations showed a sudden reconfiguration of disclination lines where the four-arm junctions of the BPII $_{[100]}$ unfold and stretch to form straight-line defects giving rise to BPI $_{[110]}$ (Fig 8D). An analysis of the director field shows that this transformation is produced by a collective and diffusion-less reconfiguration of DTCs (Fig. 8D), which was confirmed through in-situ resonance soft x-ray scattering.[38]

It has also been found that the orientation of the BP-lattice can be influenced by the curvature of interfacial boundaries. For instance, BP monodomains in LCs with high levels of chirality were formed when encapsulated in droplets, eliminating the necessity for any specific surface treatments.[33,94] The formation of monodomain crystals during the annealing process for both BPI and BPII at their respective phase temperatures was observed, but the formation of the BPII monodomain crystal structure was significantly more rapid than BPI. Additionally, during the transition from multidomain to monodomain structures, BPI experiences lattice deformation at the surface which results in a blueshift in the reflected color. However, for BPII, the shift in the reflected wavelength was not detectable (Fig. 8E). Our recent research has demonstrated that in BPs confined within microdroplets, the polymerization of the disclination network can promote the formation as well as the stabilization of monodomain BPII crystals.[39] Conversely, BPI crystals that have been stabilized with polymers fail to transition to a monodomain structure

 

(Fig. 8F). Utilizing super-resolution confocal laser scanning microscopy equipped with laser wavelengths that correspond with the periodic structure of BPs, we were able to non-invasively detect disclination network configurations and discern grain boundaries. In agreement with polarized optical microscopy, the confocal microscopy images affirm that BPI displays features characteristic of platelet crystals with bcc lattice planes of [111], [110], [200], and [211]. In contrast, BPII droplets display a single crystal with a uniform alignment of the [100] lattice plane across the entirety of the droplet.

## Conclusions

This feature article delves into the captivating world of BPs, shedding light on the impact of geometrical confinement and curvature on their structural stability, phase behavior, and the resulting photonic features. We have highlighted the primary challenges faced by BPs, including their thermal stability and polydomain crystalline features. We have also discussed potential strategies, such as polymer stabilization and nanoparticle inclusions, to expand the thermal stability of BPs, and surface patterning as a promising technique to promote single crystal growth process.

We have specifically discussed the current studies on how the interplay between surface anchoring, confinement, and curvature can affect BP structural stability and monodomain crystal formation. We have presented BP microdroplets and core-shells as two platforms that have been exploited to investigate the effect of curved confinement. These studies demonstrate that confining BPs in microdroplets can influence the crystal structure, induce single crystal formation, and expand structural stability. However, confining BPs in core-shells with both strong confinement and high curvature can destabilize BPI and force it to adopt a BPII configuration, eventually transforming to Skyrmion lattices at a high degree of confinement.

Looking ahead, the study of BPs holds great promise for further advancements in the field. In addition to the need for the development of new materials and techniques to create monodomain structures and stabilize BPs, there are still many questions that remain unexplored. In particular, current studies on the coupling effect of curvature and confinement clearly demonstrate the existing knowledge gap and offer significant scope for further exploration to expand the future applications of BP soft crystals.

The effect of flow forces on BPs is also a promising area of research. Flow forces can influence the orientation and phase behavior of LCs, potentially leading to new behaviors and properties. In this regard, experimental and computational studies of effects of shear flow, pressure-driven flow, and extensional flow on BPs could provide vital insights. This will help us to understand how to design flow systems and induce curvature to achieve desired characteristics in BP-based devices, such as improved response times or altered light manipulation properties.

The impact of the coupling of flow and curvature on BPs is another area that warrants further exploration. Although there are some studies on the effect of shear forces on the molecular arrangement and optical response of bulk BPs, far less is known about the effect of active hydrodynamic forces on chiral LCs when confined in micrometer-sized droplets. A deep understanding of the effect of the coupling of hydrodynamic forces generated in a microfluidic device and the degree of geometrical curvature on the structural reorganization and phase transitions of LCs with high level of chirality and BP droplets could be a rich area for research.

Research into the impact of the coupling of curvature and induced electric fields on BPs could lead to the development of reconfigurable devices. Further understanding of how curvature affects the structure and response time to external fields, such as electrical and light fields, could lead to the development of reconfigurable devices.

Lastly, the impact of the coupling of curvature and mechanical deformation on stabilized BPs (through either the inclusion of nanoparticles or polymerization) is an area that needs further exploration. Understanding how mechanical deformation affects the structural stability of BPs, especially when coupled with curvature, is an area that needs to be explored.

It is crucial to note that the research directions outlined above are not exhaustive, but rather represent a subset of the vast landscape awaiting exploration in the field of BPs. Continued investigations into the effects of flow, curved confinement, and external stimuli will undoubtedly contribute to the advancement and eventual commercialization of these fascinating materials in various industries, including displays, photonics, and optoelectronics. By unraveling the complexities of BPs under curved confinement, we can unlock their full potential and pave the way for exciting technological advancements in the future.

## Author contributions

J. A. M-G. and M. S. have discussed the organization and layout of the contents and all the authors jointly contributed to the writing and editing of the Feature Article.

## Conflicts of interest

There are no conflicts of interest to declare.

## Acknowledgements

This work has been supported by the National Science Foundation, Division of Materials Research, Condensed Matter Physics program, with the NSF CAREER award 2146428 and the National Science Foundation Graduate Research Fellowship under Grant No. DGE-2034711.

## Notes and references

1. P. J. de Gennes and J. S. Prost, *The Physics of Liquid Crystals*, Oxford University Press Inc., New York, Second ED., 1993.

2. P. Oswald, P. Pieranski, W. J. Goodby and G. W. Gray, *Nematic and Cholesteric Liquid Crystals Concepts and Physical Properties Illustrated by Experiments*, CRC Press, Boca Raton, 2005.

3. D. Demus, *Mol. Cryst. Liq. Cryst.*, 2007, **165**, 45–84.

4. A. Taugerbeck, and C. J. Booth, in *Design and Synthesis of Chiral Nematic Liquid Crystals*, Wiley-VCH Verlag GmbH & Co., 2014.

5. V. Ger and H. J. Wim, *Thermotropic Liquid Crystals, Fundamentals*, Springer Berlin, Heidelberg, 1988.

6. I. Dierking, *Textures of Liquid Crystals*, Wiley-VCH Verlag GmbH & Co. KGaA, 2003.

7. M. J. Stephen and J. P. Straley, *Rev. Mod. Phys.*, 1974, **46**, 617.

8. I. Dierking, *Symmetry*, 2014, **6**, 444–472.

9. J. P. F. Lagerwall and F. Giesselmann, *ChemPhysChem.*, 2006, **7**, 20–45.

10. M. Urbanski, C. G. Reyes, J. Noh, A. Sharma, Y. Geng, V. S. R. Jampani and J. P. F. Lagerwall, *J. Phys.: Condens.Matter*, 2017, **29**, DOI: 10.1088/1361-648X/aa5706.

11. H. S. Kitzerow and C. Bahr, *Chirality in Liquid Crystals,* Springer, New York, NY. 2001.

12. J. W. Goodby, *J. Mater. Chem.*, 1991, **1**, 307–318.

13. Ł. Duda, M. Czajkowski, B. Potaniec and P. Vaňkátová, *Liq. Cryst.*, 2019, **46**, 1769–1779.

14. K. George, M. Esmaeili, J. Wang, N. Taheri-Qazvini, A. Abbaspourrad and M. Sadati, *Proc. Natl. Acad. Sci. U. S. A.*, 2023, **120**, DOI: 10.1073/pnas.2220032120

15. L. L. Ma, C. Y. Li, J. T. Pan, Y. E. Ji, C. Jiang, R. Zheng, Z. Y. Wang, Y. Wang, B. X. Li and Y. Q. Lu, *Light: Sci. Appl.*, 2022, **11**, 1–24.

16. Z. Zheng, H. Hu, Z. Zhang, B. Liu, M. Li, D. H. Qu, H. Tian, W. H. Zhu and B. L. Feringa, *Nat. Photonics*, 2022, **16**, 226–234.

17. C. Duan, Z. Cheng, B. Wang, J. Zeng, J. Xu, J. Li, W. Gao, K. C. Chen Duan, Z. Cheng, B. Wang, J. Zeng, J. Xu, J. Li, W. Gao and K. Chen, *Small*, 2021, **17**, DOI: 10.1002/smll.202007306

18. D. J. Mulder, A. P. H. J. Schenning and C. W. M. Bastiaansen, *J. Mater. Chem. C*, 2014, **2**, 6695–6705.

19. M. A. Farooq, W. Wei and H. Xiong, *Langmuir*, 2020, **36**, 3072–3079.

20. H. K. Bisoyi and Q. Li, *Acc. Chem. Res.*, 2014, **47**, 3184–3195.

21. M. Ozaki, Y. Matsuhisa, H. Yoshida, R. Ozaki and A. Fujii, *Phys. Status Solidi A,* 2007, **204**, 3777–3789.

22. S. Furumi, S. Yokoyama, A. Otomo and S. Mashiko, *Appl. Phys. Lett.*, 2003, **82**, 16–18.

23. E. Dubois-violette and B. Pansu, *Mol. Cryst. Liq. Cryst. Incorporating Nonlinear Opt.,* 1988, **165**, 151–182.

24. D. C. Wright and N. D. Mermin, Rev. Mod. Phys., 1989, **61**, 385-429.

25. H. Stegemeyer, T. H. Blümel, K. Hiltrop, H. Onusseit and F. Porsch, *Liq. Cryst.,* 1985, **1**, 3–28.

 

26. T. H. Lin, Y. Li, C. T. Wang, H. C. Jau, C. W. Chen, C. C. Li, H. K. Bisoyi, T. J. Bunning and Q. Li, *Adv. Mater.*, 2013, **25**, 5050–5054.

27. I. Sage, *Liq. Cryst.*, 2011, **38**, 1551–1561.

28. J. Pišljar, S. Ghosh, S. Turlapati, N. V. S. Rao, M. Škarabot, A. Mertelj, A. Petelin, A. Nych, M. Marinčič, A. Pusovnik, M. Ravnik and I. Muševič, *Phys. Rev. X,* 2022, **12**, DOI: 10.1103/PhysRevX.12.011003.

29. J. A. N. Zasadzinski, S. Meiboom, M. J. Sammon and D. W. Berreman, *Phys. Rev. Lett.*, 1986, **57**, 364-367.

30. J. Liu, W. Liu, B. Guan, B. Wang, L. Shi, F. Jin, Z. Zheng, J. Wang, T. Ikeda and L. Jiang, *Nat. Commun.*, 2021, **12**, 1–13.

31. T. Paul and J. Saha, *Sci. Rep.*, 2020, **10**, 1–11.

32. E. P. Koistinen and P. H. Keyes, *Phys. Rev. Lett*., 1995, **74**, 4460-4463.

33. J. A. Martínez-González, Y. Zhou, M. Rahimi, E. Bukusoglu, N. L. Abbott and J. J. De Pablo, *Proc. Natl. Acad. Sci. U. S. A.,* 2015, **112**, 13195–13200.

34. M. Sadati, J. A. Martinez-Gonzalez, Y. Zhou, N. T. Qazvini, K. Kurtenbach, X. Li, E. Bukusoglu, R. Zhang, N. L. Abbott, J. P. Hernandez-Ortiz and J. J. De Pablo, *Sci. Adv.*, 2020, **6**, aba6728.

35. Y. Yang, V. Palacio-Betancur, X. Wang, J. J. De Pablo, and N. L. Abbott, *Small*, 2022, **18**, DOI: 10.1002/smll.202105835.

36. X. Li, J. A. Martínez-González, O. Guzmán, X. Ma, K. Park, C. Zhou, Y. Kambe, H. M. Jin, J. A. Dolan, P. F. Nealey and J. J. De Pablo, *Sci. Adv.*, 2019, **5**, 1-8.

37. X. Li, J. A. Martínez-González, J. P. Hernández-Ortiz, A. Ramírez-Hernández, Y. Zhou, M. Sadati, R. Zhang, P. F. Nealey and J. J. De Pablo, *Proc. Natl. Acad. Sci. U. S. A.*, 2017, **114**, 10011–10016.

38. X. Li, J. A. Martínez-González, K. Park, C. Yu, Y. Zhou, J. J. De Pablo and P. F. Nealey, *ACS Appl. Mater. Interfaces*, 2019, **11**, 9487–9495.

39. M. Sadati, J. A. Martinez-Gonzalez, A. Cohen, S. Norouzi, O. Guzmán and J. J. De Pablo, *ACS Nano*, 2021, **15**, 15972–15981.

40. I. C. Khoo and T. H. Lin, *Opt. Lett.*, 2012, **37**, 3225-3227.

41. Z. Wang, T. Xu, A. Noel, Y. Chen and T. Liu, *Soft Matter*, 2021, **17**, 4675–4702.

42. M. A. B. Pantoja, Y. Yang and N. L. Abbott, *Liq. Cryst.,* 2019, **46**, 1925–1936.

43. C. H. Chang, M. J. Lee and W. Lee, *Biomed. Opt. Express*, 2017, **8**, 1712–1720.

44. K. Orzechowski, M. M. Sala-Tefelska, M. W. Sierakowski, T. R. Woliński, O. Strzeżysz and P. Kula, *Opt. Express*, 2019, **27**, 14270-14282.

45. V. Sridurai, M. Mathews, C. V. Yelamaggad and G. G. Nair, *ACS Appl. Mater. Interfaces*, 2017, **9**, 39569–39575.

46. M. Sadati, A. I. Apik, J. C. Armas-Perez, J. Martinez-Gonzalez, J. P. Hernandez-Ortiz, N. L. Abbott and J. J. De Pablo, *Adv. Funct. Mater.*, 2015, **25**, 6050–6060.

47. M. Sadati, H. Ramezani-Dakhel, W. Bu, E. Sevgen, Z. Liang, C. Erol, M. Rahimi, N. Taheri Qazvini, B. Lin, N. L. Abbott, B. Roux, M. L. Schlossman and J. J. De Pablo, *J. Am. Chem. Soc.,* 2017, **139**, 3841–3850.

48. H. Ramezani-Dakhel, M. Sadati, R. Zhang, M. Rahimi, K. Kurtenbach, B. Roux and J. J. De Pablo, *ACS Cent. Sci.*, 2017, **3**, 1345–1349.

49. S. Norouzi, J. A. Martinez-González and M. Sadati, *Biosensors*, 2022, **12**, 313-323.

50. J. A. Martínez-González, X. Li, M. Sadati, Y. Zhou, R. Zhang, P. F. Nealey and J. J. De Pablo, *Nat. Commun.,* 2017, **8**, DOI: 10.1038/ncomms15854.

51. E. Otón, H. Yoshida, P. Morawiak, O. Strzeżysz, P. Kula, M. Ozaki and W. Piecek, *Sci. Rep.,* 2020, **10**, 1–8.

52. T. H. Lin, Y. Li, C. T. Wang, H. C. Jau, C. W. Chen, C. C. Li, H. K. Bisoyi, T. J. Bunning and Q. Li, *Adv. Mater.*, 2013, **25**, 5050–5054.

53. C. W. Chen, C. T. Hou, C. C. Li, H. C. Jau, C. T. Wang, C. L. Hong, D. Y. Guo, C. Y. Wang, S. P. Chiang, T. J. Bunning, I. C. Khoo and T. H. Lin, *Nat. Commun.,* 2017, **8**, 1–8.

54. Y. Chen and S. T. Wu, *Appl. Phys. Lett.*, 2013, **102**, DOI: 10.1063/1.4803922.

55. J. I. Fukuda and S. Žumer, *Phys. Rev. E: Stat., Nonlinear Soft Matter Phys.,* 2011, **82**, DOI: 10.1103/PhysRevE.82.061702

56. J. I. Fukuda and S. Žumer, *Nat. Commun.,* 2011, **2**, 1–5.

57. J. I. Fukuda and S. Žumer, *Phys. Rev. Lett.*, 2010, **104**, DOI: 10.1103/PhysRevLett.104.017801.

58. J. I. Fukuda and S. Žumer, *Phys. Rev. Lett.*, 2011, **106**, DOI: 10.1103/PhysRevLett.106.097801.

59. J. I. Fukuda, A. Nych, U. Ognysta, S. Žumer and I. Muševič, *Sci. Rep.,* 2018, **8**, 1–8.

60. A. Nych, J. I. Fukuda, U. Ognysta, S. Žumer, and I. Muševič, *Nat. Phys.*, 2017, **13**, 1215–1220.

61. A. Duzgun, C. Nisoli, C. J. O. Reichhardt and C. Reichhardt, *Soft Matter*, 2020, **16**, 3338–3343.

62. A. I. Feldman, P. P. Crooker and L. M. Goh, *Phys. Rev. A*, 1987, **35**, 491-495 .

63. T. Blümel and H. Stegemeyer, *Liq. Cryst.*, 1987, **3**, 195–201.

64. J. Fukuda and S. Žumer, *Liq. Cryst.*, 2010, **37**, 875–882.

65. M. Chen, Y. H. Lin, P. J. Chen, S. Y. Ni and H. S. Chen, *Opt. Mater. Express*, 2016, **6**, 1003–1010.

66. E. Bukusoglu, J. A. Martinez-Gonzalez, X. Wang, Y. Zhou, J. J. De Pablo and N. L. Abbott, *Soft Matter*, 2017, **13**, 8999–9006.

67. J. I. Fukuda and S. Žumer, *Phys. Rev. E*, 2011, **84**, DOI: 10.1103/PhysRevE.84.040701.

68. H. Ramezani-Dakhel, M. Sadati, M. Rahimi, A. Ramirez-Hernandez, B. Roux and J. J. De Pablo, *J. Chem. Theory Comput.,* 2017, **13**, 237–244.

69. M. Sadati, H. Ramezani-Dakhel, W. Bu, E. Sevgen, Z. Liang, C. Erol, M. Rahimi, N. Taheri Qazvini, B. Lin, N. L. Abbott, B. Roux, M. L. Schlossman and J. J. De Pablo, *J. Am. Chem. Soc.*, 2017, **139**, 3841–3850.

70. J. Shechter, N. Atzin, A. Mozaffari, R. Zhang, Y. Zhou, B. Strain, L. M. Oster, J. J. De Pablo and J. L. Ross, *Langmuir,* 2020, **36**, 7074–7082.

71. K. Peddireddy, S. Čopar, K. V. Le, I. Muševič, C. Bahr and Venkata. S. R. Jampani, *Proc. Natl. Acad. Sci. U. S. A.*, 2021, **14**, DOI: 10.1073/pnas.2011174118.

72. A. V. Dubtsov, S. V. Pasechnik, D. V. Shmeliova, A. Sh. Saidgaziev, E. Gongadze, A. Iglič and S. Kralj, *Soft Matter*, 2018, **14**, 9619–9630.

73. Z. Sumer and A. Striolo, *Soft Matter*, 2019, **15**, 3914–3922.

74. M. Sadati, Y. Zhou, D. Melchert, A. Guo, J. A. Martinez-Gonzalez, T. F. Roberts, R. Zhang and J. J. De Pablo, *Soft Matter*, 2017, **13**, 7465–7472.

75. S. A. Khadem, M. Bagnani, R. Mezzenga, and A.D. Rey, *Nat. Commun.,* 2020, **11**, 1-10.

76. R. J. Atkin and I. W. Stewart, J. *Non-Newtonian Fluid Mech.*, 2004, **119**, 105–113.

77. O. A. Gomes, C. A. R. Yednak, B. V. H. V. Da Silva and R. T. Teixeira-Souza, *Phys. Rev. E*, 2018, **97**, DOI: 10.1103/PhysRevE.97.022703.

78. L. Hou, S. Chen, X. Zhou and Z. Zhang, *Liq. Cryst.*, 2020, **47**, 950–957.

79. J. Jeong, L. Kang, Z. S. Davidson, P. J. Collings, T. C. Lubensky and A. G. Yodh, *Proc. Natl. Acad. Sci. U. S. A.,* 2015, **112**, 1837–1884.

80. V. Tomar, S. I. Hernández, N. L. Abbott, J. P. Hernández-Ortiz and J. J. De Pablo, *Soft Matter*, 2012, **8**, 8679–8689.

81. M. N. Krakhalev, A. P. Gardymova, O. O. Prishchepa, V. Y. Rudyak, A. V. Emelyanenko, J. H. Liu and V. Y. Zyryanov, *Sci. Rep.*, 2017, **7**, 1–10.

82. D. Seč, S. Čopar and S. Žumer, *Nat. Commun.,* 2014, **5**, 1–7.

 

83. L. Tran, M. O. Lavrentovich, G. Durey, A. Darmon, M. F. Haase, N. Li, D. Lee, K. J. Stebe, R. D. Kamien and T. Lopez-Leon, *Phys. Rev. X*, 2017, **7**, DOI: 10.1103/PhysRevX.7.041029.

84. F. Xu and P. P. Crooker, *Phys. Rev. E*, 1997, **56**, 6853–6860.

85. S. S. Lee, S. K. Kim, J. C. Won, Y. H. Kim and S. H. Kim, *Angew. Chem., Int. Ed. Engl.*, 2015, **54**, 15266–15270.

86. E. Bukusoglu, X. Wang, Y. Zhou, J. A. Martínez-González, M. Rahimi, Q. Wang, J. J. De Pablo and N. L. Abbott, *Soft Matter*, 2016, **12**, 8781–8789.

87. Y. Zhou, E. Bukusoglu, J. A. Martínez-González, M. Rahimi, T. F. Roberts, R. Zhang, X. Wang, N. L. Abbott and J. J. De Pablo, *ACS Nano*, 2016, **10**, 6484–6490.

88. A. P. Gardymova, M. N. Krakhalev and V. Y. Zyryanov, *Molecules*, **25,** 10.3390/molecules25071740.

89. J. Yoshioka, F. Ito and Y. Tabe, *Soft Matter*, 2016, **12**, 2400–2407.

90. G. Posnjak, S. Čopar and I. Muševič, *Sci. Rep.*, 2016, **6**, 1–10.

91. A. Darmon, M. Benzaquen, D. Seč, S. Čopar, O. Dauchot and T. Lopez-Leon, *Proc. Natl. Acad. Sci. U. S. A.,* 2016, **113**, 9469–9474.

92. S. Norouzi, A. Tavera-Vazquez, J. Ramirez-De Arellano, D. S. Kim, T. Lopez-Leon, J. J. De Pablo, J. A. Martinez-Gonzalez and M. Sadati, *ACS Nano*, 2022, **16,** 15894–15906.

93. L. Tran, M. O. Lavrentovich, G. Durey, A. Darmon, M. F. Haase, N. Li, D. Lee, K. J. Stebe, R. D. Kamien and T. Lopez-Leon, *Phys. Rev. X*, 2017, **7**, DOI: 10.1103/PhysRevX.7.041029.

94. E. Bukusoglu, X. Wang, J. A. Martinez-Gonzalez, J. J. De Pablo and N. L. Abbott, *Adv. Mater.,* 2015, **27**, 6892–6898.

95. V. Palacio-Betancur, J. C. Armas-Pérez, S. Villada-Gil, N. L. Abbott, J. P. Hernández-Ortiz and J. J. De Pablo, *Soft Matter*, 2020, **16**, 870–880.

96. H. Kikuchi, M. Yokota, Y. Hisakado, H. Yang and T. Kajiyama*, Nat. Mater.,* 2002, **1**, 64–68.

97. F. Castles, F. V. Day, S. M. Morris, D. H. Ko, D. J. Gardiner, M. M. Qasim, S. Nosheen, P. J. W. Hands, S. S. Choi, R. H. Friend and H. J. Coles, *Nat. Mater.*, 2012, **11**, 599–603.

98. F. Castles, S. M. Morris, J. M. C. Hung, M. M. Qasim, A. D. Wright, S. Nosheen, S. S. Choi, B. I. Outram, S. J. Elston, C. Burgess, L. Hill, T. D. Wilkinson and H. J. Coles, *Nat. Mater*., 2014, **13**, 817–821.

99. Q. Yan, Z. Wei, P. Lin, Z. Cheng, M. Pu, Z. Huang, and W. Lin, *Opt. Mater. Express*, 2018, **8**, 1536–1550.

100. R. Kizhakidathazhath, H. Higuchi, Y. Okumura and H. Kikuchi, *J. Mol. Liq.,* 2018, **262**, 175–179.

101. C. Y. Fan, H. C. Jau, T. H. Lin, F. C. Yu, T. H. Huang, C. Liu and N. Sugiura, *J. Disp. Technol.,* 2011, **7**, 615–618.

102. S. Y. Jo, S. W. Jeon, B. C. Kim, J. H. Bae, F. Araoka and S. W. Choi, *ACS Appl Mater Interfaces*, 2017, 9, 8941–8947.

103. M. Ravnik, G. P. Alexander, J. M. Yeomans, and S. Žumer, *Proc. Natl. Acad. Sci. U. S. A.,* 2011, **108,** 5188-5192.

104. M. A. Gharbi, S. Manet, J. Lhermitte, S. Brown, J. Milette, V. Toader, M. Sutton and L. Reven, *ACS Nano*, 2016, **10**, 3410–3415.

105. H. Yoshida, Y. Tanaka, K. Kawamoto, H. Kubo, T. Tsuda, A. Fujii, S. Kuwabata, H. Kikuchi and M. Ozaki, *Appl. Phys. Express*, 2009, **2**, 1-3.

106. J. D. Lin, Y. L. D. Ho, L. Chen, M. Lopez-Garcia, S. A. Jiang, M. P. C. Taverne, C. R. Lee and J. G. Rarity, *ACS Omega*, 2018, **3**, 15435–15441.

107. J. I. Fukuda, *Phys. Rev. E*, 2010, **82**, 1-5.

108. Z. G. Zheng, C. L. Yuan, W. Hu, H. Krishna Bisoyi, M. J. Tang, Z. Liu, P. Z. Sun, W. Q. Yang, X. Q. Wang, D. Shen, Y. Li, F. Ye, Y. Q. Lu, G. Li, Q. Li, *Adv. Mater.*, 2017, **29**, DOI: 10.1002/adma.201703165.

 

109. X. W. Xu, X. W. Zhang, D. Luo, and H. T. Dai, *Opt. Express,* 2015, **23,** 32267-32273.

110. T. Emeršič, K. Bagchi, J. A. Martinez-Gonzalez, X. Li, J. J. De Pablo, and P. Nealey, *Adv. Func. Mater.* 2022, **32,** 1-9.

111. J. Xiang and O. Lavrentovich, *Appl. Phys. Lett.,* 2013, **103,** DOI: 10.1063/1.4817724**.**

112. K. Lee, U. Tohgha, T. Bunning, M. McConney, and N. Godman, *Nanomaterials,* 2021, **48,** DOI: 10.3390/nano12010048.

113. E. Karatairi, B. Rozic, Z. Kutnjak, V. Tzitzios, G. Nounesis, G. Cordoyiannis, J. Thoen, C. Glorieux, and S. Kralj, *Phys. Rev. E, 2010.* **81,** DOI: 10.1103/PhysRevE.81.041703.

 